

## Retarded Stellar Dynamo in Tidally Deformed M Dwarfs

Song Wang<sup>1,2,7†\*</sup>, Wenbo Li<sup>3,7†</sup>, Henggeng Han<sup>1</sup>, Dali Kong<sup>3,4\*</sup>, Jifeng Liu<sup>1,2,4,5\*</sup>, and Xinlin Zhao<sup>6</sup>

<sup>1</sup>Key Laboratory of Optical Astronomy, National Astronomical Observatories, Chinese Academy of Sciences, Beijing 100101, China;;

<sup>2</sup>Institute for Frontiers in Astronomy and Astrophysics, Beijing Normal University, Beijing, 102206, China;;

<sup>3</sup>Shanghai Astronomical Observatory, Chinese Academy of Sciences, Shanghai 200030, China;;

<sup>4</sup>School of Astronomy and Space Science, University of Chinese Academy of Sciences, Beijing 100049, China;;

<sup>5</sup>New Cornerstone Science Laboratory, National Astronomical Observatories, Chinese Academy of Sciences, Beijing, 100012, China;;

<sup>6</sup>Department of Physics, Chongqing University, Chongqing 400044, China;

<sup>†</sup>Equally contributed to this work

Received January 11, 2023; accepted April 6, 2023

Current studies of stellar dynamos primarily focus on spherical stars, leaving their behavior in distorted stars largely unexplored. We utilize stars of varying distortions to examine the relation between stellar cycle periods ( $P_{\text{cyc}}$ ) and rotational periods ( $P_{\text{rot}}$ ), which are closely linked to dynamo processes. By analyzing a sample of tidally distorted M dwarfs in cataclysmic variables, we identify an anti-correlation between  $P_{\text{cyc}}$  and  $P_{\text{rot}}$ , in contrast to the lack of such a relation in single M dwarfs. This means that stars with greater deformation have longer cycle periods, suggesting variations in dynamo behavior under non-spherical geometries. Our numerical simulations further reveal that, the thermal convection weakens in highly distorted stars, and subsequently, the differential rotation is also reduced. These effects may lengthen the conversion timescale between poloidal and toroidal magnetic fields, potentially explaining the newly discovered  $P_{\text{cyc}}-P_{\text{rot}}$  relation in cataclysmic variables.

**Cataclysmic variable stars, Stellar magnetic dynamo, Stellar cycle**

**PACS number(s):**

**Citation:** Wang S, et al, Retarded Stellar Dynamo in Tidally Deformed M Dwarfs, Sci. China-Phys. Mech. Astron. **66**, 000000 (2023), <https://doi.org/??>

### 1 Introduction

Most studies of dynamo processes, which govern the generation and evolution of magnetic fields, focus on spherically symmetric stars. It is therefore compelling to investigate how dynamo mechanisms operate in non-spherical stars, where the deformation caused by rapid rotation and tidal forces from companion stars may alter the structure of the convection zone and the profiles of differential rotation. Stellar activity cycle is thought to be a result of dynamo processes [1, 2]. Thus, examining the relation

between cycle periods ( $P_{\text{cyc}}$ ) and rotation periods ( $P_{\text{rot}}$ ) in both spherical and non-spherical stars offers a promising approach to probing dynamo processes across different stellar geometries.

Pioneering observational and theoretical studies have shown that the  $P_{\text{cyc}}-P_{\text{rot}}$  relation serves as a key constraint on dynamo models [3-8]. For example, for stars with rotation periods shorter than  $\approx 10$  days, a weak positive relation between  $P_{\text{cyc}}$  and  $P_{\text{rot}}$  is observed for F, G, and K dwarfs in the  $P_{\text{cyc}}/P_{\text{rot}}$  vs.  $1/P_{\text{rot}}$  diagram on a log-log scale [4, 9, 10], but no such relation has been identified for M dwarfs [10-13]. The different behavior of the relations was explained as that the dynamos in M stars differ from those in F, G, and K stars.

\*Corresponding authors (Song Wang, email: [songw@bao.ac.cn](mailto:songw@bao.ac.cn); Dali Kong, email: [dkong@shao.ac.cn](mailto:dkong@shao.ac.cn); Jifeng Liu, email: [jfliu@bao.ac.cn](mailto:jfliu@bao.ac.cn))

For M stars, which are fully or nearly fully convective, their magnetic fields are likely generated by a distributed dynamo, with magnetic cycles potentially governed by turbulent diffusion and meridional circulation [14].

To investigate dynamo behavior in distorted stars, we compiled a sample of M stars, comprising single dwarfs, dwarfs in wide binaries, and those in close binaries, and examined their  $P_{\text{cyc}}-P_{\text{rot}}$  relations. For close binaries, we focused on cataclysmic variable (CV) systems, each consisting of a white dwarf and a tidally distorted late-type dwarf, which offer a clear advantage over normal close binaries, as both the rotation periods and cycle periods can be unambiguously attributed to the dwarf component. The paper is organized as follows. In Section 2, we describe the construction of the sample and data analysis, including the compilation of stars with measured cycle and rotation periods from the literature. Section 3 presents the relations between  $\log(P_{\text{cyc}}/P_{\text{rot}})$  and  $\log(1/P_{\text{rot}})$  for M dwarfs. In Section 4, we introduce a binary model to investigate the impact of tidal deformation on stellar thermal convection. Finally, Section 5 provides discussion and conclusions of our findings.

## 2 Sample selection and data analysis

We compiled a sample of M dwarfs including single stars, wide binaries, and close binaries. First, we collected stellar cycle and rotation periods for 89 M singles and M wide binaries from previous studies (e.g., refs. [10, 12–20]), which mainly used long-term photometric light curves and chromospheric activity monitoring to identify stellar activity cycles. Although [11] presented a set of cycle periods for M single stars, those periods have been thought as short secondary cycles and were therefore not included in our sample. Cross-matching with SIMBAD identified six M single stars as binaries; they were categorized to the wide binary sample (see Supplementary Material). This leads to 65 M single stars and 24 M stars in wide binaries. Then, we searched for close binaries including M dwarfs, specifically defined as CV systems having orbital periods shorter than 0.3 days. In these tidally locked systems, the orbital period equals the rotational period of the M dwarf. The sample is drawn mainly from [5, 21–24], yielding 23 M stars in CVs. The full M-dwarf sample is shown in Figure 1. Detailed information on their rotation and cycle periods is listed in Tables S1–S3.

Generally, in previous studies, standard time-series analysis methods such as (Generalized) Lomb-Scargle periodograms, Fourier transforms, and Phase Dispersion Minimization were employed to detect long-term cyclic variations. For CVs in our sample, two additional methods were also used to extract cycle periods from light curve data: (1)

tracking orbital period variations using the observed-minus-calculated ( $O-C$ ) method [25], and (2) measuring variations in the intervals between outbursts in accreting systems [21]. The underlying physical explanation is that magnetic field variations in the convective layers of the cool star (i.e., the M dwarf) during an activity cycle cause the star to expand and contract within a quadrupole-deformed Roche potential [26, 27]. Such radius variations can alter the star's moment of inertia and further produce both detectable apsidal motion and orbital period variations with the same timescale as the magnetic cycle, even in circular orbits [21]. Simultaneously, since the cool star fills its Roche lobe, the changes in radius also result in variation in the mass transfer rate. This, in turn, alters the luminosity of the accretion disk surrounding the white dwarf primary [21, 22].

We noted that an alternative explanation for the recurring outbursts in CV systems is the disk instability model, which attributes dwarf nova outbursts to thermal and viscous instabilities in the accretion disk, triggered by hydrogen ionization. However, in old novae and novalike binaries, the accretion disks are typically smaller and more stable than those of dwarf novae. More importantly, the approximately regular recurrence times observed in some CVs cannot be explained by the disk instability model. Therefore, in this study, we interpreted the periods measured from variations in outburst intervals as stellar activity cycle periods. Fortunately, only four CVs in our sample have their cycle periods determined through the intervals between recurring outbursts.

Similar to our sun, stellar activity cycles can be multiple [9]. At moderate rotation rates ( $\approx 10-20$  days), some stars exhibit cycles on two sequences, which were explained as two stellar dynamos operating simultaneously in different shear layers [28, 29]. Different detection methods may also lead to different estimations of cycle lengths. For example, the cycle lengths unveiled by direct tracking of polarity switches are sometimes significantly shorter than those derived from chromospheric activity monitoring [30]. The cycles identified by CoRoT [31] or Kepler [17] missions are much shorter ( $\lesssim 2-3$  years) than classical activity cycle lengths. It should be noted that cycle periods below about 1–2 years, especially those derived from records with approximately yearly gaps, may be highly uncertain [9]. Therefore, in following analysis, we consider only cycles longer than 2 years, leaving 54 single stars, 23 wide binaries, and 23 CVs (Figure 1). For stars with multiple reported cycle measurements, we adopted the most recent result to ensure accuracy.

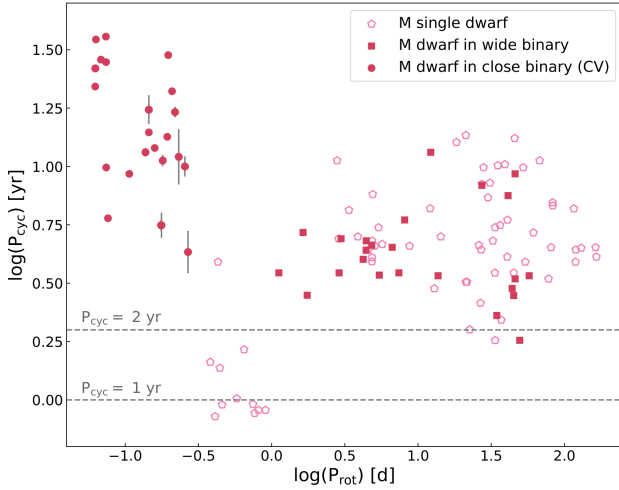


**Figure 1**  $P_{\text{cyc}}$  versus  $P_{\text{rot}}$  in log–log scale for M dwarfs. Filled dots represent stars in close binaries (i.e., CVs), while filled squares represent stars in wide binaries. Open pentagons represent single stars. The two horizontal dashed lines represent stars with cycle periods of 1 and 2 years, respectively.

### 3 Results: new $P_{\text{cyc}}-P_{\text{rot}}$ relation

Previous studies have reported no correlation between  $P_{\text{cyc}}$  and  $P_{\text{rot}}$  for single M dwarfs. The derived slopes for the  $\log(P_{\text{cyc}}/P_{\text{rot}})$  versus  $\log(1/P_{\text{rot}})$  relationship in these studies include:  $1.03 \pm 0.04$  [11],  $1.10 \pm 0.03$  [12], and  $1.01 \pm 0.06$  [13], etc. In contrast, our analysis of M dwarfs in CV systems yields a significantly steeper slope. The best-fit linear relation between  $\log(P_{\text{cyc}}/P_{\text{rot}})$  and  $\log(1/P_{\text{rot}})$  for these M-star CVs (Figure 2) yields

$$\log(P_{\text{cyc}}/P_{\text{rot}}) = (1.59 \pm 0.05) \times \log(1/P_{\text{rot}}) + (3.19 \pm 0.04). \quad (1)$$

This reveals a clear connection between  $P_{\text{cyc}}$  and  $P_{\text{rot}}$ :

$$P_{\text{cyc}} \propto P_{\text{rot}}^{-0.59}, \quad (2)$$

suggesting faster-rotating stars tend to maintain longer cycle periods (see Figure 1).

We also performed a third-order polynomial fit to the relation between  $\log(P_{\text{cyc}}/P_{\text{rot}})$  and  $\log(1/P_{\text{rot}})$  for the whole sample:

$$\log(P_{\text{cyc}}/P_{\text{rot}}) = (3.284 \pm 0.049) + (1.173 \pm 0.042)x + (0.230 \pm 0.050)x^2 + (0.074 \pm 0.028)x^3, \quad (3)$$

where  $x = \log(1/P_{\text{rot}})$ . This fit clearly reveals variations in the relation across different stellar systems. The contrasting behavior between M dwarfs in close binaries and single M dwarfs suggests differences in their underlying dynamo mechanisms.

## 4 Simulation

In close binary systems, stars cannot be treated as spherical fluids as single stars, due to the asymmetric deformation caused by rotation and tidal forces from their companions. This deformation not only redistributes stellar mass but also changes internal physical fields and thermal status of the star, which may influence magnetic dynamo processes and be reflected in the observed relation between  $P_{\text{cyc}}$  and  $P_{\text{rot}}$ . Given that stars in close binaries exhibit longer activity cycle periods, a plausible explanation is that their dynamo actions are altered, requiring longer timescales to accumulate sufficient energy to drive a magnetic cycle.

We constructed a binary model to study the effects of the asymmetrical deformation of the figure of stars, due to rotation and tidal forcing from their companions, on thermal convection inside them (Figure 3). In this physical model, star A of mass  $M$  is tidally locked to its companion, star B, which is simplified as a point mass  $m_s$ . The origin  $O$  of the coordinate system is set at the center of mass of star A, while the mass point B is located on the  $x$ -axis at  $\mathbf{r}_s = r_s \hat{\mathbf{x}}$ . Star A rotates along the  $z$ -axis with a constant angular velocity  $\boldsymbol{\Omega} = \Omega \hat{\mathbf{z}}$ . The  $y$ -axis is perpendicular to the  $xOz$  plane pointing inward. To focus on the effects of asymmetric stellar figures on thermal convection, star A was modelled by an internally heated Boussinesq fluid of constant density  $\rho_0$  by constant heat sources  $Q_h$ . The material properties of star A, such as the kinematic viscosity  $\nu$ , the thermal diffusivity  $\kappa$ , the thermal expansion coefficient  $\alpha_T$ , and the specific heat capacity of constant pressure  $c_p$ , are assumed to be constant as well. The dynamics of thermal convection in star A is then governed by the following dimensional equations in the co-rotating frame of reference [32]:

$$\rho_0 \left( \frac{\partial \mathbf{u}}{\partial t} + \mathbf{u} \cdot \nabla \mathbf{u} + 2\boldsymbol{\Omega} \times \mathbf{u} \right) = -\nabla p + \rho [g_0 - \boldsymbol{\Omega} \times (\boldsymbol{\Omega} \times \mathbf{r}) + g_T] + \rho_0 \nu \nabla^2 \mathbf{u}, \quad (4)$$

$$\frac{\partial T}{\partial t} + \mathbf{u} \cdot \nabla T = \kappa \nabla^2 T + \frac{Q_h}{c_p \rho_0}, \quad \text{and} \quad (5)$$

$$\nabla \cdot \mathbf{u} = 0, \quad (6)$$

where  $\mathbf{u}$  is the velocity of a fluid parcel marked by a position vector  $\mathbf{r}$ ,  $p$  represents the hydrodynamic pressure, and  $T$  denotes the temperature. The density related to the buoyancy is determined as  $\rho = \rho_0(1 - \alpha_T T)$ . Besides the self-gravity  $g_0$ , the contributions of the centrifugal force  $-\boldsymbol{\Omega} \times (\boldsymbol{\Omega} \times \mathbf{r})$  due to rotation and the tidal force  $g_T$  imposed by the mass point B are also considered in the buoyancy in this physical model. The no-slip boundary condition for velocity,

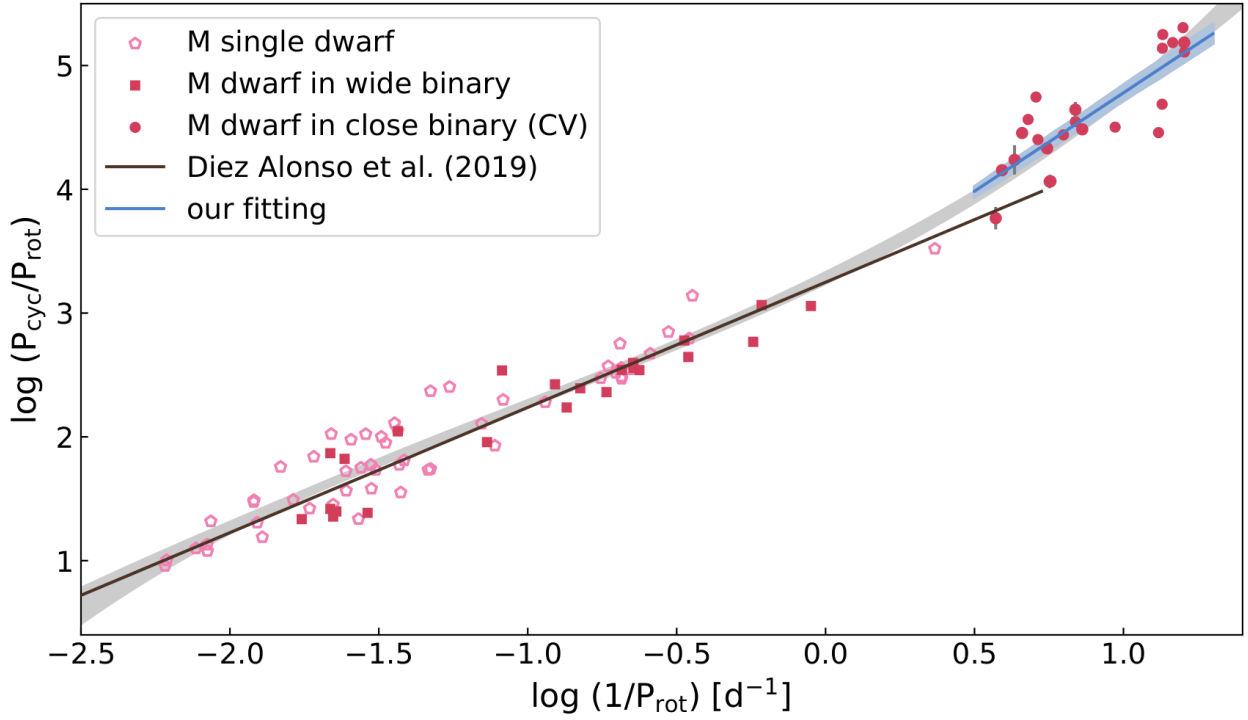


**Figure 2**  $P_{\text{cyc}}/P_{\text{rot}}$  versus  $1/P_{\text{rot}}$  in log–log scale for M stars. Open pentagons represent single stars. Filled dots represent stars in close binaries (i.e., CVs), while filled squares represent stars in wide binaries. The solid black line is the fitting from literature [13] for single M dwarfs with a slope of  $1.01 \pm 0.06$ . The blue line represents our fitting using M dwarfs in close binaries, with a slope of  $1.59 \pm 0.05$ , and the shaded blue region indicates the  $1\sigma$  uncertainty of the linear fit. The shaded gray region denotes the  $1\sigma$  uncertainty of the polynomial fit to the whole sample.

the isothermal boundary condition for temperature and the equipotential equilibrium condition

$$\mathbf{u} = \mathbf{0}, \quad T = 0, \quad U = \text{constant}, \quad (7)$$

were adopted at the boundary surface of star A. Here, the total potential  $U$  is the sum of the self-gravity potential, the centrifugal potential, and the tide-generating potential.

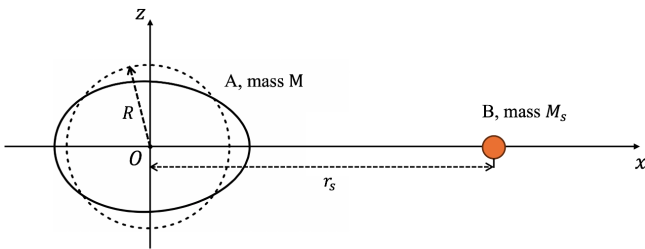


**Figure 3** Sketch of a binary system under the asymmetrical deformation. Star A of mass  $M$  and the companion B of mass  $m_s$  are tidally locked to each other. The dashed circle denotes the original spherically symmetric shape of star A of radius  $R$ , while the solid curve represents its asymmetrically deformed figure due to its fast rotation and the tidal forcing from the companion B. In this physical model the companion B is simplified as a mass point. The distance between the barycenters of A and B is  $r_s$ .

The key step to study thermal convection within star A is the determination of its deformed figure shaped by the rotation and tidal forcing imposed by the mass point B. As star A

is tidally locked to its companion B, the figure of A is taken to be that in the hydrostatic state in the co-rotating frame of reference. The non-perturbative iteration method is employed to obtain the time-independent figure of star A in the hydrostatic state [33–36]. The accuracy of this iteration method has been investigated [37]. According to the iteration method, the deformed figure is controlled by the two dimensionless parameters  $q_{\text{rot}} = \frac{\Omega^2 R^3}{GM}$  and  $q_{\text{tid}} = -\frac{3m_s R^3}{Mr_s^3}$ , where  $G$  is the universal gravitational constant and  $R$  denotes the supposed spherical radius of star A when getting rid of rotation and tides (i.e., the radius of the dashed circle in Figure 3). As the Keplerian orbit is adopted in this tide-locked system, only  $q_{\text{rot}}$  is free, which can be re-expressed as

$$q_{\text{rot}} = \left(1 + \frac{m_s}{M}\right) \left(\frac{R}{r_s}\right)^3. \quad (8)$$

As the mass  $m_s$  of the companion B becomes relatively larger than that of star A or the ratio of the spherical radius  $R$  to the distance  $r_s$  between these two objects becomes larger, the value of  $q_{\text{rot}}$  increases, resulting in a more heavily deformed figure of star A. The volume covered by the deformed surface calculated by the iteration method for any given  $q_{\text{rot}}$  is required to be the same as that of the sphere of radius  $R$  such that the conservation of mass of star A of constant density is guaranteed.

Once the deformed figures of star A are obtained, direct numerical simulations of thermal convection were performed using the finite element method. The numerical method and the overall code have been successfully used and validated in modeling of thermal convection in rotating oblate spheroids flattened by the effects of fast rotation alone [38–41]. It's clear that the dynamics of thermal convection in star A is characterized by the Ekman number  $Ek$  which measures the relative importance of the viscous force and the Coriolis force, the Prandtl number  $Pr$  which is the ratio of the kinematic viscosity  $\nu$  to the thermal diffusivity  $\kappa$ , the Rayleigh number  $Ra$  which measures the ratio of destabilizing buoyancy to stabilizing processes, and the value of  $q_{\text{rot}}$  which decides the deformed figure of star A at hydrostatic state in the rotating frame of reference. The thermal convection of stars is in the regime of inertial convection, which is marked by the asymptotically small Ekman number  $Ek \ll 1$  and the sufficiently small Prandtl number  $Pr < 1$ . In all the numerical simulation cases, the Ekman number and the Prandtl number are fixed at  $Ek = 10^{-4}$  and  $Pr = 5 \times 10^{-3}$  (for computational feasibility), respectively, in order to investigate the effects of asymmetrical deformation of different degree, measured quantitatively by values of  $q_{\text{rot}}$ , on thermal convection in star A. Since the velocity decreases to zero in the very thin boundary layer, the computational domain is discretized using an unstructured tetrahedral mesh of second order with a typical fine mesh size  $O(R\sqrt{Ek})$  near the boundary surface. More specifically, in the thin region of depth  $0.02R$  adjacent to the boundary, the max size of mesh is set to be below  $R\sqrt{Ek}$ .

We conducted numerical simulations for two sets of physical configurations: one representing a slightly deformed spherical-like figure with  $m_s/M = 50$  and  $r_s/R = 15$ , and the other representing a significantly deformed asymmetrical figure with  $m_s/M = 50$  and  $r_s/R = 10$ . Taking the critical Rayleigh number  $Ra_c = 1.63$  of thermal convection within the undeformed sphere as the baseline [39], we found that  $Ra_c$  increases by 6% to 1.74 for the spherical-like figure with  $q_{\text{rot}} = 0.015$ , while by 31% to 2.13 for the heavily deformed figure with  $q_{\text{rot}} = 0.051$  (Table 1). This increasing tendency of  $Ra_c$  with  $q_{\text{rot}}$  shows a stronger repression of thermal convection as a star undergoes heavier asymmetrical deformation caused by rotation and tidal forces. It is also indicated (in Figure 4) that the velocity field at the onset of thermal convection becomes non-axisymmetrically stretched when the figure of a star becomes significantly deformed. It should be noted that the definition of the Rayleigh number  $Ra$  here is identical to that of the stratification number  $St$  in [39].

Since the critical Rayleigh number  $Ra_c$  increases as the figure undergoes heavier asymmetric deformation, it is revealed (in Figure 5) that the strength of time-averaged thermal convection in stars of close binaries with significantly deformed

figures becomes slightly weaker than that in spherical-like stars at the same level of supercritical convection (e.g., at  $Ra = 10Ra_c$ ). The total kinetic energy, dimensionalized by the unit  $\rho_0 R^5 \Omega^2$ , of the time-averaged azimuthal velocity  $\hat{\phi} \cdot \bar{U}$  normalized by  $R\Omega$  decreases slightly from 0.0068 at  $q_{\text{rot}} = 0.015$  to 0.0060 at  $q_{\text{rot}} = 0.051$ . Here  $\rho_0$  is the density in the hydrostatic state,  $\bar{U}$  represents the time-averaged velocity, and  $\hat{\phi}$  denotes the conventional longitudinal direction in the polar spherical coordinates. Subsequently, as shown in Figure 6, the mean zonal flows  $\langle \bar{U} \rangle$  averaged from the results of Figure 5 over the longitude at the spherical surface of radius  $r = 0.85R$ , simulated at  $Ra = 10Ra_c$  with two different values of  $q_{\text{rot}}$ , also indicate that the differential rotation tends to weaken as stellar deformation increases.

## 5 Discussion and conclusions

We compiled a sample of M dwarfs as single stars or components of binary systems. These stars, spanning a range of tidal distortions, were used to investigate the relationship between stellar cycle periods ( $P_{\text{cyc}}$ ) and rotation periods ( $P_{\text{rot}}$ ), which are key observables linked to stellar dynamo processes.

From our analysis of tidally distorted M dwarfs in CVs, we identified a strong anti-correlation between  $P_{\text{cyc}}$  and  $P_{\text{rot}}$ , characterized by  $\log(P_{\text{cyc}}/P_{\text{rot}}) \propto (\log(1/P_{\text{rot}}))^{1.59 \pm 0.05}$ . This contrasts with the nearly linear relation found in single M dwarfs (slope  $\approx 1.01$ – $1.10$ ). Our result means that stars experiencing stronger tidal distortion tend to have longer magnetic cycles, suggesting modifications to the dynamo mechanism under non-spherical geometries.

To understand the physical origin of the varying  $P_{\text{cyc}}-P_{\text{rot}}$  relation, we constructed a binary model to study the influence of asymmetric stellar deformation on thermal convection. Our simulations show that thermal convection weakens in highly distorted stars, and subsequently, the differential rotation is also reduced. These, in turn, may increase the timescale for magnetic field conversion between poloidal and toroidal components, offering a plausible explanation for the newly identified  $P_{\text{cyc}}-P_{\text{rot}}$  relation observed in CVs.

We calculated the dimensionless parameters  $q_{\text{rot}}$  and  $q_{\text{tid}}$  for our M-star sample, by compiling stellar and orbital parameters for wide and close binaries from previous studies, including stellar types, component masses, orbital periods, etc (see Tables S4 and S5 for details). As in our simulation,  $q_{\text{rot}}$  and  $q_{\text{tid}}$  were calculated following  $q_{\text{rot}} = (1 + \frac{m_s}{M})(\frac{R}{r_s})^3$  and  $q_{\text{tid}} = -\frac{3m_s R^3}{M r_s^3}$ , respectively. Here  $M$  represents the mass of the observed star, corresponding to the brighter component in normal binaries or the non-compact star (i.e., the M dwarf) in binaries with compact companions.  $R$  is the spherical radius of the observed star when getting rid of rotation

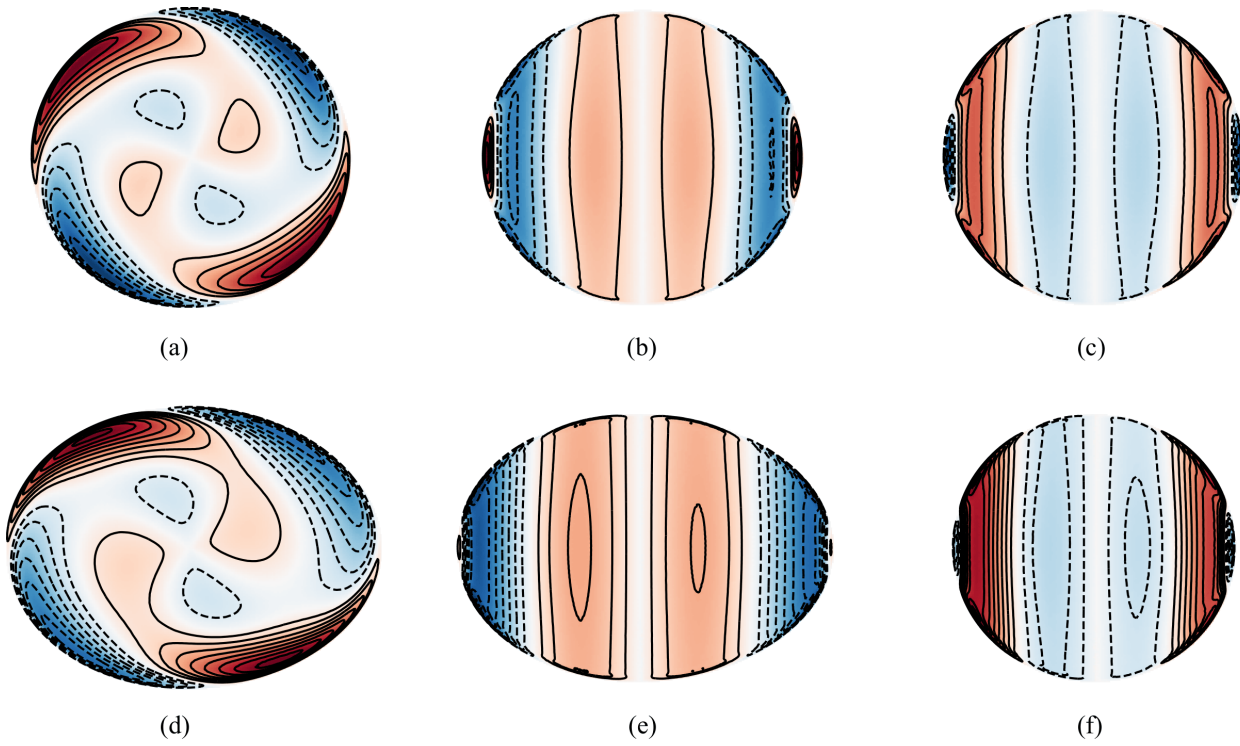


**Figure 4** Contours of the azimuthal component  $\hat{\phi} \cdot \mathbf{u}$  of flows at the onset of thermal convection computed via direct numerical simulation. The top row represents the numerical results in the slightly deformed figure with  $q_{\text{rot}} = 0.015$ , while the bottom row demonstrates the numerical results in the heavily deformed figure with  $q_{\text{rot}} = 0.051$ . The panels (a) and (d) are sliced in the  $xOy$  plane, (b) and (e) in the  $xOz$  plane, and (c) and (f) in the  $yOz$  plane. Other physical parameters are referred to Table 1.

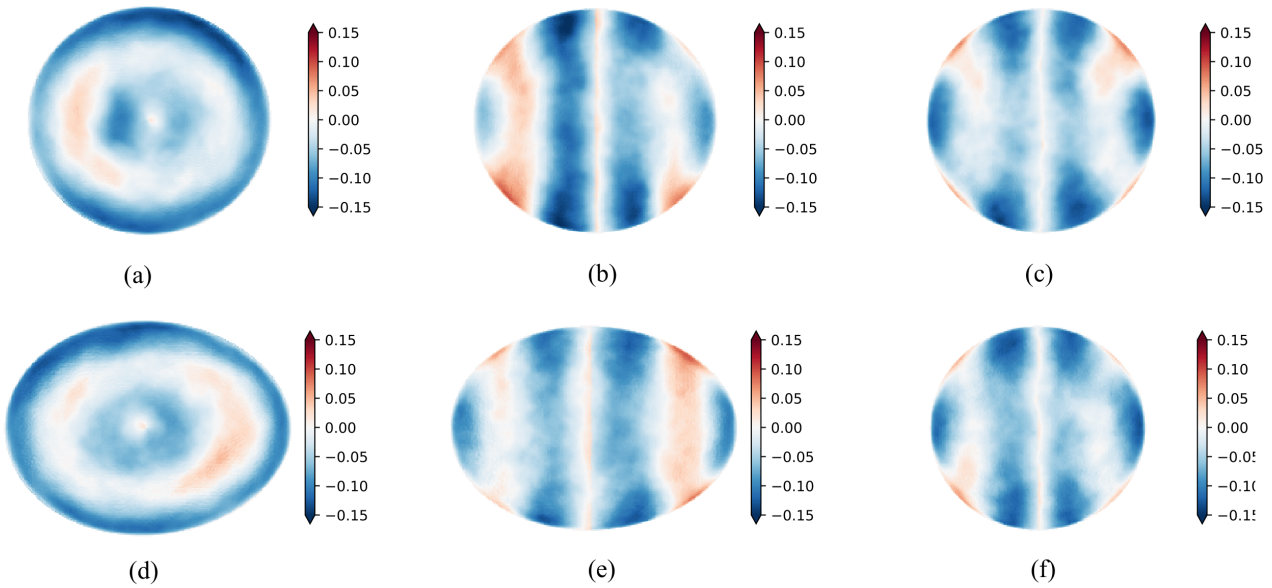


**Figure 5** Contours of the time-averaged azimuthal velocity  $\hat{\phi} \cdot \overline{\mathbf{U}}$  of turbulent flows via simulation. The top panels represent the numerical results in the slightly deformed figure with  $q_{\text{rot}} = 0.015$ , while the bottom panels describe the numerical results in the heavily deformed figure with  $q_{\text{rot}} = 0.051$ . The unit of velocity is  $R\Omega$ , with  $R$  and  $\Omega$  being the spherical radius and strength of angular velocity of rotation, respectively. The Rayleigh number is fixed at  $Ra = 10Ra_c$ , respectively, in these numerical results. Other physical parameters are referred to Table 1. The panels (a) and (d) are sliced in the  $xOy$  plane, (b) and (e) in the  $xOz$  plane, and (c) and (f) in the  $yOz$  plane.

and tides, estimated with  $R/R_\odot \approx (M/M_\odot)^{0.9}$  [42].  $m_s$  is the mass of the companion star. The binary separation  $r_s$  was derived by Kepler's third law:  $r_s^3 = (M + m_s)P_{\text{orb}}^2$ . Figure 7 shows the distribution of our binary sample in the  $q_{\text{tid}}$  versus  $q_{\text{rot}}$  diagram, compared to the two sets of simulations. Most M dwarfs in our CV sample exhibit deformation levels exceeding that represented by the simulation with  $q_{\text{rot}} = 0.051$ . In addition, as an example, Figure S1 presents mesh plots for the wide binary GJ 1054 A and the close binary DQ Her, which clearly illustrates distinct stellar geometries.

In the Parker kinematic migratory dynamo model [1], the cycle period  $P_{\text{cyc}}$  is proportional to the dynamo number  $D$  by  $P_{\text{cyc}} \sim D^{-2/3}$  [4]. The dynamo number is given by  $D = \alpha \Delta \Omega d^3 / \eta^2 \sim \alpha \Delta \Omega$  [43], where  $d$  is the characteristic convection length scale,  $\eta$  is the turbulent magnetic diffusivity,  $\alpha$  represents the helicity,  $\Omega$  is the angular velocity, and  $\Delta \Omega$  denotes differential rotation. Thus, the cycle period  $P_{\text{cyc}}$  scales as  $[\eta^2 / (\alpha \Delta \Omega)]^{3/2}$ .

Our simulations indicated that deformed stars exhibit suppressed thermal convection. This suppression has two competing effects on the dynamo process. On one hand, it reduces the kinematic helicity  $\alpha$  (which originates from the convection-rotation interaction) and weakens the mean zonal flows, implying a decrease in the differential rotation shear  $\Delta \Omega$ . Both observations [44] and theoretical [45] studies have reported that low-mass stars with weaker convection possess reduced differential rotation. On the other hand, the turbulent magnetic diffusivity  $\eta$  is also expected to decrease in such stars, which would enhance the dynamo efficiency in generating magnetic field. Consequently, the resulting cycle period depends on which of these two effects dominates: the reduction of  $\alpha$  and  $\Delta \Omega$  versus the decrease in  $\eta$ . In this study, the observed new  $P_{\text{cyc}}-P_{\text{rot}}$  relation, together with our simulations, suggests that the reduction in  $\alpha$  and  $\Delta \Omega$  is the dominant process, leading to a lengthening of the activity cycle.

Additional observational evidences also suggest the link between dynamo processes and stellar deformation. For example, magnetically active close binaries (which, we note, are not classified as CVs in this work), often exhibit starspots concentrated at preferred longitudes [46-49], which can be explained by the formation of clusters of flux tube eruptions at specific longitudes, driven by tidal forces and deviations of stellar structure from spherical symmetry [50, 51]. Moreover, such a connection between dynamo retardment and stellar deformation may help explain the well-known supersaturation phenomenon, where stellar activity decreases with increasing rotational velocity, as observed in X-ray, chromospheric, and photometric emissions [52-55], particularly in binary systems. Close binary systems thus provide a cosmic laboratory to probe dynamo mechanisms under extreme stel-

lar geometries.

**Table 1** Critical Rayleigh numbers in different physical configurations.

$Ek$	$Pr$	$m_s/M$	$r_s/R$	$q_{\text{rot}}$	$Ra_c$
		—	—	0	1.63*
$10^{-4}$	$5 \times 10^{-3}$	50	15	0.015	1.74
		50	10	0.051	2.13

\*The critical Rayleigh number  $Ra_c = 1.63$  for rotating spheres at the given  $Ek$  and  $Pr$  is referred to [39], in which the Rayleigh number is denoted as the stratification number.

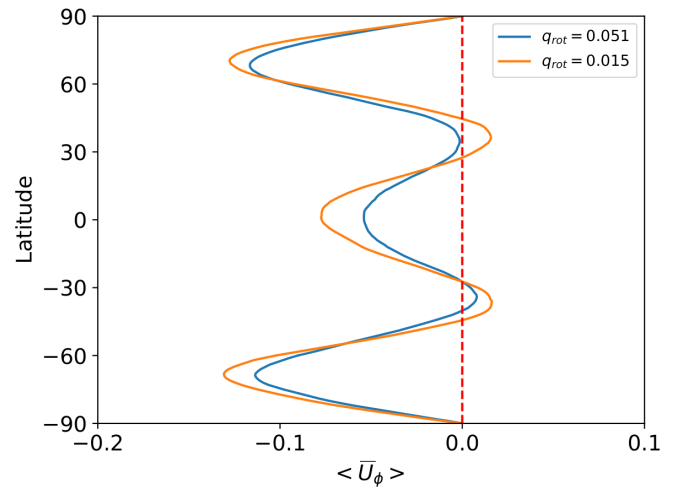


**Figure 6** Mean zonal flows at the spherical surface of radius  $r = 0.85R$  (centered at the origin) for two representative values of  $q_{\text{rot}}$ . The Rayleigh number, Ekman number and Prandtl number are fixed at  $Ra = 10Ra_c$ ,  $Ek = 10^{-4}$  and  $Pr = 5 \times 10^{-3}$ , respectively. It can be seen that the mean zonal flows tend to weaken as stellar deformation increases.

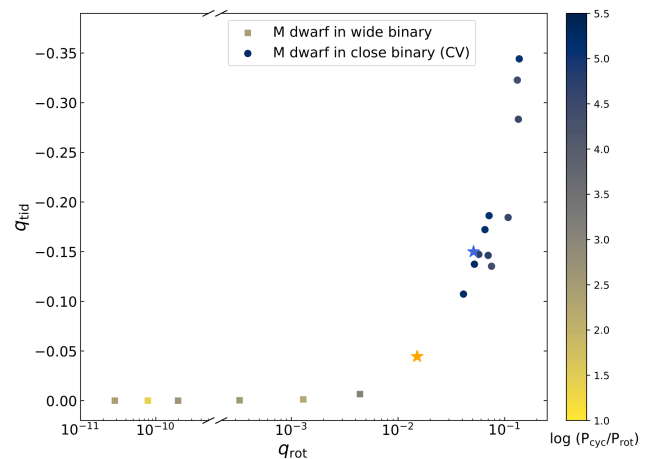


**Figure 7** Distribution of the M binary sample in the  $q_{\text{tid}}$  versus  $q_{\text{rot}}$  diagram. The orange and blue asterisks represent the two simulations with  $q_{\text{rot}} = 0.015$  and  $0.051$ , respectively. The colorbar represents the  $\log(P_{\text{cyc}}/P_{\text{rot}})$  values.

*J.F.L. was funded by the National Natural Science Foundation of China (NSFC) under grant number 12588202. S.W. was funded by the National Key Research and Development Program of China under grant number 2023YFA1607901, the Strategic Priority Program of the Chinese Academy of Sciences under grant number XDB1160302, the NSFC under grant number 12273057, and science research grants from the China Manned Space Project. W.B.L. was funded by the NSFC under grant number 12403070 and the Shanghai Post-doctoral Excellence Program under number 2023000137. D.L.K. was funded by the NSFC under grant numbers 12425306 and 12250013. J.F.L. was also supported by the New Cornerstone Science Foundation through the New Cornerstone Investigator Program and the XPLORER PRIZE.*

**Conflict of interest** The authors declare that they have no conflict of interest.

- 1 E. N. Parker, *Astrophys. J.* **122**, 293 (1955).
- 2 S. L. Baliunas, R. A. Donahue, W. H. Soon, J. H. Horne, J. Frazer, L. Woodard-Eklund, M. Bradford, L. M. Rao, O. C. Wilson, Q. Zhang, W. Bennett, J. Briggs, S. M. Carroll, D. K. Duncan, D. Figueroa, H. H. Lanning, T. Misch, J. Mueller, R. W. Noyes, D. Poppe, A. C. Porter, C. R. Robinson, J. Russell, J. C. Shelton, T. Soyumer, A. H. Vaughan, and J. H. Whitney, *Astrophys. J.* **438**, 269 (1995).
- 3 R. W. Noyes, N. O. Weiss, and A. H. Vaughan, *Astrophys. J.* **287**, 769 (1984).
- 4 S. L. Baliunas, E. Nesme-Ribes, D. Sokoloff, and W. H. Soon, *Astrophys. J.* **460**, 848 (1996).
- 5 S. H. Saar and A. Brandenburg, *Astrophys. J.* **524**, 295 (1999).
- 6 A. Strugarek, P. Beaudoin, P. Charbonneau, A. S. Brun, and J. D. do Nascimento, *Science* **357**, 185 (2017), arXiv: [1707.04335](#).
- 7 J. Warnecke, *Astron. Astrophys.* **616**, A72 (2018), arXiv: [1712.01248](#).
- 8 M. Viviani, J. Warnecke, M. J. Käpylä, P. J. Käpylä, N. Olsper, E. M. Cole-Kodikara, J. J. Lehtinen, and A. Brandenburg, *Astron. Astrophys.* **616**, A160 (2018), arXiv: [1710.10222](#).
- 9 K. Oláh, Z. Kolláth, T. Granzer, K. G. Strassmeier, A. F. Lanza, S. Järvinen, H. Korhonen, S. L. Baliunas, W. Soon, S. Messina, and G. Cutispoto, *Astron. Astrophys.* **501**, 703 (2009), arXiv: [0904.1747](#).
- 10 A. Suárez Mascareño, R. Rebolo, and J. I. González Hernández, *Astron. Astrophys.* **595**, A12 (2016), arXiv: [1607.03049](#).
- 11 I. S. Savanov, *Astronomy Reports* **56**, 716 (2012).
- 12 A. Suárez Mascareño, R. Rebolo, J. I. González Hernández, B. Toledo-Padrón, M. Perger, I. Ribas, L. Affer, G. Micela, M. Damasso, J. Maldonado, E. González-Alvarez, G. Leto, I. Pagano, G. Scandariato, A. Sozzetti, A. F. Lanza, L. Malavolta, R. Claudi, R. Cosentino, S. Desidera, P. Giacobbe, A. Maggio, M. Rainer, M. Esposito, S. Benatti, M. Pedani, J. C. Morales, E. Herrero, M. Lafarga, A. Rosich, and M. Pinamonti, *Astron. Astrophys.* **612**, A89 (2018), arXiv: [1712.07375](#).
- 13 E. Díez Alonso, J. A. Caballero, D. Montes, F. J. de Cos Juez, S. Dreizler, F. Dubois, S. V. Jeffers, S. Lalitha, R. Naves, A. Reiners, I. Ribas, S. Vanaverbeke, P. J. Amado, V. J. S. Béjar, M. Cortés-Contreras, E. Herrero, D. Hidalgo, M. Kürster, L. Logie, A. Quirrenbach, S. Rau, W. Seifert, P. Schöfer, and L. Tal-Or, *Astron. Astrophys.* **621**, A126 (2019), arXiv: [1810.03338](#).
- 14 M. Küker, G. Rüdiger, K. Olah, and K. G. Strassmeier, *Astron. Astrophys.* **622**, A40 (2019), arXiv: [1804.02925](#).
- 15 P. Robertson, M. Endl, W. D. Cochran, and S. E. Dodson-Robinson, *Astrophys. J.* **764**, 3 (2013), arXiv: [1211.6091](#).
- 16 K. Vida, L. Kriskovics, and K. Oláh, *Astronomische Nachrichten* **334**, 972 (2013), arXiv: [1306.6845](#).
- 17 K. Vida, K. Oláh, and R. Szabó, *Mon. Not. R. Astron. Soc.* **441**, 2744 (2014), arXiv: [1404.4359](#).
- 18 K. Oláh, Z. Kővári, K. Petrovay, W. Soon, S. Baliunas, Z. Kolláth, and K. Vida, *Astron. Astrophys.* **590**, A133 (2016), arXiv: [1604.06701](#).
- 19 E. Distefano, A. C. Lanzafame, A. F. Lanza, S. Messina, and F. Spada, *Astron. Astrophys.* **591**, A43 (2016), arXiv: [1604.01917](#).
- 20 E. Distefano, A. C. Lanzafame, A. F. Lanza, S. Messina, and F. Spada, *Astron. Astrophys.* **606**, A58 (2017), arXiv: [1706.07938](#).
- 21 A. Bianchini, *Astron. J.* **99**, 1941 (1990).
- 22 A. Bianchini, in *Cataclysmic Variable Stars*, (edited by N. Vogt), volume 29 of *Astronomical Society of the Pacific Conference Series*, 284 (1992).
- 23 T. Ak, M. T. Ozkan, and J. A. Mattei, *Astron. Astrophys.* **369**, 882 (2001).
- 24 H. Ritter and U. Kolb, *Astron. Astrophys.* **404**, 301 (2003), arXiv: [astro-ph/0301444](#).
- 25 H. R. Richman, J. H. Applegate, and J. Patterson, *Publ. Astron. Soc. Pac.* **106**, 1075 (1994).
- 26 J. H. Applegate and J. Patterson, *Astrophys. J. Lett.* **322**, L99 (1987).
- 27 B. Warner, *Nature* **336**, 129 (1988).
- 28 E. Böhm-Vitense, *Astrophys. J.* **657**, 486 (2007).
- 29 A. Brandenburg, S. Mathur, and T. S. Metcalfe, *Astrophys. J.* **845**, 79 (2017), arXiv: [1704.09009](#).
- 30 A. Morgenthaler, P. Petit, J. Morin, M. Aurière, B. Dinttrans, R. Konstantinova-Antova, and S. Marsden, *Astronomische Nachrichten* **332**, 866 (2011), arXiv: [1109.3982](#).
- 31 C. E. Ferreira Lopes, I. C. Leão, D. B. de Freitas, B. L. Canto Martins, M. Catelan, and J. R. De Medeiros, *Astron. Astrophys.* **583**, A134 (2015), arXiv: [1508.06194](#).
- 32 S. Chandrasekhar, *Hydrodynamic and hydromagnetic stability* (1961).
- 33 W. B. Hubbard, *The Astrophysical Journal* **756**, L15 (2012).
- 34 W. B. Hubbard, *The Astrophysical Journal* **768**, 43 (2013).
- 35 S. M. Wahl, W. B. Hubbard, and B. Militzer, *Icarus* **282**, 183 (2017).
- 36 S. M. Wahl, M. Parisi, W. M. Folkner, W. B. Hubbard, and B. Militzer, *The Astrophysical Journal* **891**, 42 (2020).
- 37 W. Hubbard, G. Schubert, D. Kong, and K. Zhang, *Icarus* **242**, 138 (2014).
- 38 D. Kong, *Physical Review Fluids* **7**, 074803 (2022).
- 39 W. Li and D. Kong, *Physical Review Fluids* **7**, 103502 (2022).
- 40 W. Li and D. Kong, *Physical Review Fluids* **8**, L011501 (2023).
- 41 W. Li and D. Kong, *Phys. Rev. Fluids* **9**, 113502 (2024).
- 42 J. Patterson, *Astrophys. J. Suppl. Ser.* **54**, 443 (1984).
- 43 W. H. Soon, S. L. Baliunas, and Q. Zhang, *Astrophys. J. Lett.* **414**, L33 (1993).
- 44 J. R. Barnes, A. Collier Cameron, J.-F. Donati, D. J. James, S. C. Marsden, and P. Petit, *Mon. Not. R. Astron. Soc.* **357**, L1 (2005), arXiv: [astro-ph/0410575](#).
- 45 L. L. Kitchatinov and S. V. Oleskoy, *Mon. Not. R. Astron. Soc.* **411**, 1059 (2011), arXiv: [1009.3734](#).
- 46 K. Olah, E. Budding, H. L. Kim, and P. B. Etzel, *Astron. Astrophys.* **291**, 110 (1994).
- 47 G. W. Henry, J. A. Eaton, J. Hamer, and D. S. Hall, *Astrophys. J. Suppl. Ser.* **97**, 513 (1995).
- 48 P. A. Heckert, G. V. Maloney, M. C. Stewart, J. I. Ordway, A. Hickman, and M. Zeilik, *Astron. J.* **115**, 1145 (1998).
- 49 K. Oláh, K. G. Strassmeier, and M. Weber, *Astron. Astrophys.* **389**, 202 (2002).
- 50 V. Holzwarth and M. Schüssler, *Astron. Astrophys.* **405**, 291 (2003), arXiv: [astro-ph/0304496](#).
- 51 V. Holzwarth and M. Schüssler, *Astron. Astrophys.* **405**, 303 (2003), arXiv: [astro-ph/0304498](#).
- 52 N. J. Wright, J. J. Drake, E. E. Mamajek, and G. W. Henry, *Astrophys. J.* **743**, 48 (2011), arXiv: [1109.4634](#).
- 53 D. Chahal, R. de Grijs, D. Kamath, and X. Chen, *Mon. Not. R. Astron. Soc.* **514**, 4932 (2022), arXiv: [2206.05505](#).
- 54 Y. Ding, S. Zhang, H. Han, W. Cui, S. Wang, M. Fang, and Y. Gao, *Astrophys. J.* **976**, 243 (2024), arXiv: [2410.15039](#).
- 55 J. Yu, C. Gehan, S. Hekker, M. Bazot, R. H. Cameron, P. Gaulme, T. R. Bedding, S. J. Murphy, Z. Han, Y.-S. Ting, J. Tayar, Y. Chen, L. Gi-

- zon, J. Nordhaus, and S. Bi, *Nature Astronomy* **9**, 1045 (2025), arXiv: [2505.19967](https://arxiv.org/abs/2505.19967).
- 56 B. J. Wargelin, S. H. Saar, G. Pojmański, J. J. Drake, and V. L. Kashyap, *Mon. Not. R. Astron. Soc.* **464**, 3281 (2017), arXiv: [1610.03447](https://arxiv.org/abs/1610.03447).
- 57 P. Godon, E. M. Sion, K. Levay, A. P. Linnell, P. Szkody, P. E. Barrett, I. Hubeny, and W. P. Blair, *Astrophys. J. Suppl. Ser.* **203**, 29 (2012), arXiv: [1210.1118](https://arxiv.org/abs/1210.1118).
- 58 A. W. Shafter and J. N. Holland, *Publ. Astron. Soc. Pac.* **115**, 1105 (2003).
- 59 L. Pilarčík, M. Wolf, P. A. Dubovský, K. Hornoch, and L. Kotková, *Astron. Astrophys.* **539**, A153 (2012).
- 60 A. H. Knight, A. Ingram, M. Middleton, and J. Drake, *Mon. Not. R. Astron. Soc.* **510**, 4736 (2022), arXiv: [2201.02188](https://arxiv.org/abs/2201.02188).
- 61 B. W. Borges, R. Baptista, C. Papadimitriou, and O. Giannakis, *Astron. Astrophys.* **480**, 481 (2008), arXiv: [0711.3660](https://arxiv.org/abs/0711.3660).
- 62 J. G. Greenhill, K. M. Hill, S. Dieters, K. Fienberg, M. Howlett, A. Meijers, A. Munro, and C. Senkbeil, *Mon. Not. R. Astron. Soc.* **372**, 1129 (2006), arXiv: [astro-ph/0602331](https://arxiv.org/abs/astro-ph/0602331).
- 63 X. Zhao, S. Wang, X. Li, Y. Xiang, F. Xu, S. Gu, B. Du, and J. Liu, *Astrophys. J.* **963**, 160 (2024), arXiv: [2401.06991](https://arxiv.org/abs/2401.06991).
- 64 R. Baptista, B. W. Borges, H. E. Bond, F. Jablonski, J. E. Steiner, and A. D. Grauer, *Mon. Not. R. Astron. Soc.* **345**, 889 (2003), arXiv: [astro-ph/0307514](https://arxiv.org/abs/astro-ph/0307514).
- 65 R. Baptista, F. Jablonski, E. Oliveira, S. Vrielmann, P. A. Woudt, and M. S. Catalán, *Mon. Not. R. Astron. Soc.* **335**, L75 (2002), arXiv: [astro-ph/0207438](https://arxiv.org/abs/astro-ph/0207438).
- 66 M. Paegert, K. G. Stassun, K. A. Collins, J. Pepper, G. Torres, J. Jenkins, J. D. Twicken, and D. W. Latham, arXiv e-prints arXiv:2108.04778 (2021), arXiv: [2108.04778](https://arxiv.org/abs/2108.04778).
- 67 V. Šimon, *Mon. Not. R. Astron. Soc.* **463**, 1342 (2016).

## Supplementary Materials

### A Period values for our sample of M dwarfs.

During sample construction, we cross-matched M single stars with SIMBAD and found six objects catalogued as spectroscopic binaries: BD-022198, GJ182, HIP1910, HIP23200, HIP36349, V1428Aql. They were moved to the wide binary sample.

Tables S1, S2, and S3 list the period estimates for the M single dwarfs, M dwarfs in wide binaries, and M dwarfs in close binaries, respectively.

The methods for cycle period measurements listed in these tables are as follows. LC: light curve; CL: chromospheric line. LS: Lomb Scargle; GLS: Generalized Lomb Scargle; BTFT: Bilinear Time-Frequency Transformation; PDM: Phase Dispersion Minimization; STFT: Short-Term Fourier Transform; FT: Fourier Transform; DFT: Discrete Fourier Transform; IO: intervals between outbursts.

The references for period measurements listed in these tables include: (1) [13]; (2) [16]; (3) [12]; (4) [10]; (5) [14]; (6) [15]; (7) [18]; (8) [19]; (9) [20]; (10) [17]; (11) [56]; (12) [22]; (13) [5]; (14) [23]; (15) [24]; (16) [21]; (17) [57]; (18) [58]; (19) [59]; (20) [60]; (21) [61]; (22) [62]; (23) [25]; (24) [63]; (25) [64]; (26) [65]; (27) [66]; (28) [9]; (29) [28]; (30) [67].

For stars with multiple cycle measurements,  $P_{\text{cycl}}$  represents the most recent result. For MV Lyr, RW Tri, and V603 Aql, the referenced cycle periods are 11–12 years, 8–14 years, and 15–20 years, respectively; we used the median value of each range as the cycle period and half of the interval as its uncertainty.

### B Derived parameters for our binary sample including M dwarfs.

Tables S4 and S5 list derived parameters for wide and close binaries with M-dwarf components, including stellar types, component masses, orbital periods, etc.

**Table S1** Period measurements for M-type single stars.

Name	R.A. (deg)	Decl. Type (deg)	$P_{\text{rot}}$ (day)	$\log(\frac{1}{P_{\text{rot}}})$ (1/day)	$P_{\text{cyc1}}$ (day)	$P_{\text{cyc2}}$ (day)	$\log(\frac{P_{\text{cyc1}}}{P_{\text{rot}}})$	$\log(\frac{P_{\text{cyc2}}}{P_{\text{rot}}})$	Method <sup>a</sup>	Ref.
ANSex	153.07362	-3.74566	M2	21.6	-1.33	1168	—	1.73	—	LC(LS) (1)
BD+044157	293.666	4.58251	M0	12.9	-1.11	1095	—	1.93	—	LC(LS) (1)
EYDra	274.06991	54.1727	M1	0.46	0.34	348	—	2.88	—	LC(FT) (2)
FIVir	176.93499	0.80456	M4	163.0	-2.21	1642	—	1.0	—	LC(LS) (1)
GJ162	62.15583	33.63704	M1	32.4	-1.51	1752	—	1.73	—	CL(GLS) (3)
GJ176	70.7324	18.95817	M2	40.8	-1.61	2153	—	1.72	—	LC(GLS) (4)
GJ184	75.84959	53.12847	M0	45.0	-1.65	1277	—	1.45	—	CL(GLS) (3)
GJ2	1.29537	45.78657	M1	21.2	-1.33	1168	—	1.74	—	CL(GLS) (3)
GJ205	82.86415	-3.67723	M1	33.5	-1.52	1278	—	1.58	—	LC(BTFT) (5)
GJ2066	124.03326	1.30257	M2	40.7	-1.61	1496	—	1.57	—	LC(LS) (1)
GJ229	92.64423	-21.86463	M1	27.3	-1.44	3066	—	2.05	—	LC(GLS) (4)
GJ270	109.88031	32.83009	M2	30.0	-1.48	2687	—	1.95	—	CL(GLS) (5,6)
GJ273	111.85208	5.22579	M3	115.9	-2.06	2409	—	1.32	—	LC(GLS) (4)
GJ285	116.16738	3.55247	M4	2.8	-0.45	3869	—	3.14	—	LC(GLS) (4)
GJ328	133.78176	1.5465	M0	33.6	-1.53	2000	—	1.77	—	CL(GLS) (5,6)
GJ3367	86.82486	-0.01355	M0	12.1	-1.08	2411	—	2.3	—	LC(BTFT) (5)
GJ358	144.9432	-41.06756	M2	26.0	-1.42	1680	—	1.81	—	LC(BTFT) (5)
GJ382	153.07362	-3.74566	M2	21.2	-1.33	4964	—	2.37	—	LC(GLS) (4)
GJ3822	210.58177	13.68964	M0	18.3	-1.26	4635	—	2.4	—	CL(GLS) (3)
GJ3997	258.95874	19.00004	M0	37.0	-1.57	803	—	1.34	—	CL(GLS) (3)
GJ3998	259.00265	11.05767	M1	33.6	-1.53	657	—	1.29	—	CL(GLS) (3)
GJ4057	276.26998	24.63458	M0	26.7	-1.43	949	—	1.55	—	CL(GLS) (3)
GJ4306	343.99936	17.81105	M1	27.0	-1.43	1606	—	1.77	—	CL(GLS) (3)
GJ431	172.9438	-41.04644	M3	14.3	-1.16	1826	—	2.11	—	LC(BTFT) (5)
GJ447	176.93499	0.80456	M4	165.1	-2.22	1496	—	0.96	—	LC(GLS) (4)
GJ479	189.46757	-52.00148	M3	22.5	-1.35	730	—	1.51	—	LC(GLS) (4)
GJ514	202.49911	10.37716	M1	28.0	-1.45	3613	—	2.11	—	LC(GLS) (4)
GJ526	206.4324	14.89152	M4	52.3	-1.72	3613	—	1.84	—	LC(GLS) (4)
GJ551	217.42894	-62.67949	M5	83.2	-1.92	2482	—	1.47	—	LC(GLS) (4)
GJ581	229.86178	-7.72227	M3	130.0	-2.11	1633	—	1.1	—	CL(GLS) (5,6)

<sup>a</sup>NOTES. LC: light curve; CL: chromospheric line. LS: Lomb Scargle; GLS: Generalized Lomb Scargle; BTFT: Bilinear Time-Frequency Transformation; PDM: Phase Dispersion Minimization; STFT: Short-Term Fourier Transform; FT: Fourier Transform; DFT: Discrete Fourier Transform; IO: intervals between outbursts.

**Table S1** Continued. Period measurements for M-type single stars.

Name	R.A. (deg)	Decl. (deg)	Type	$P_{\text{rot}}$ (day)	$\log(\frac{1}{P_{\text{rot}}})$ (1/day)	$P_{\text{cyc1}}$ (day)	$P_{\text{cyc2}}$ (day)	$\log(\frac{P_{\text{cyc1}}}{P_{\text{rot}}})$	$\log(\frac{P_{\text{cyc2}}}{P_{\text{rot}}})$	Method	Refs.
GJ588	233.05388	-41.27559	M2	61.3	-1.79	1899	—	1.49	—	LC(GLS)	(4)
GJ625	246.3526	54.3041	M2	77.8	-1.89	1204	—	1.19	—	CL(GLS)	(3)
GJ628	247.57524	-12.66259	M4	119.3	-2.08	1606	—	1.13	—	LC(GLS)	(4)
GJ674	262.16644	-46.89519	M3	35.0	-1.54	3686	—	2.02	—	LC(GLS)	(4)
GJ729	282.45568	-23.83624	M3	2.87	-0.46	1790	—	2.8	—	LC(BTFT)	(5)
GJ740	284.50057	5.90812	M0	36.3	-1.56	2044	—	1.75	—	CL(GLS)	(3)
GJ803	311.28972	-31.3409	M1	4.86	-0.69	1753	—	2.56	—	LC(BTFT)	(5)
GJ832	323.39156	-49.009	M1	45.7	-1.66	4818	—	2.02	—	LC(GLS)	(4)
GJ846	330.54281	1.40023	M0	31.0	-1.49	3102	—	2.0	—	LC(GLS)	(4)
GJ849	332.4181	-4.64074	M3	39.2	-1.59	3723	—	1.98	—	LC(GLS)	(4)
GJ890	347.08146	-15.40994	M0	0.43	0.37	1424	—	3.52	—	LC(BTFT)	(5)
HD197481	311.28972	-31.3409	M1	4.9	-0.69	2774	—	2.75	—	LC(GLS)	(4)
HD95735	165.83414	35.96988	M2	54.0	-1.73	1424	—	1.42	—	LC(LS)	(7)
HIP102409	311.28972	-31.3409	M1	4.84	-0.68	1428	—	2.47	—	LC(LS/PDM)	(8,9)
HIP107345	326.12551	-60.97747	M0	4.55	-0.66	1600	—	2.55	—	LC(LS/PDM)	(8,9)
HIP17695	56.84725	-1.97221	M3	3.88	-0.59	1826	—	2.67	—	LC(BTFT)	(5)
HIP23309	75.19637	-57.25707	M0	8.74	-0.94	1666	—	2.28	—	LC(LS/PDM)	(8,9)
ILAqr	343.31972	-14.2637	M3	81.0	-1.91	1642	—	1.31	—	LC(LS)	(1)
KIC03541346	290.48612	38.62535	M0	0.91	0.04	330	—	2.56	—	LC(STFT)	(10)
KIC04819564	286.35546	39.91813	M0	0.38	0.42	530	—	3.14	—	LC(STFT)	(10)
KIC04953358	298.77777	40.09237	M1	0.65	0.19	600	—	2.97	—	LC(STFT)	(10)
KIC05791720	292.07429	41.07007	M3	0.77	0.12	320	—	2.62	—	LC(STFT)	(10)
KIC06675318	286.34714	42.11492	M0	0.58	0.24	370	—	2.81	—	LC(STFT)	(10)
KIC07592990	286.36267	43.24619	M0	0.44	0.35	500	—	3.05	—	LC(STFT)	(10)
KIC08314902	296.89699	44.23397	M0	0.81	0.09	330	—	2.61	—	LC(STFT)	(10)
KIC10515986	282.33037	47.72497	M1	0.75	0.13	350	—	2.67	—	LC(STFT)	(10)
KIC11087527	293.5498	48.68472	M0	0.41	0.39	310	—	2.88	—	LC(STFT)	(10)
LP 816-60	313.13757	-16.97472	M4	67.6	-1.83	3869	—	1.76	—	LC(GLS)	(4)
OTSer	230.47055	20.97775	M1	3.37	-0.53	2372	—	2.85	—	LC(LS)	(1)
ProxCen	217.42894	-62.67949	M3	83.0	-1.92	2557	—	1.49	—	LC(LS)	(11)
TWA2	167.30747	-30.02777	M2	4.85	-0.69	1489	—	2.49	—	LC(LS/PDM)	(8,9)
TWA25	183.878	-39.81183	M1	5.06	-0.7	1666	—	2.52	—	LC(LS/PDM)	(8,9)
TYC5832-0666-1	353.12859	-12.2643	M0	5.69	-0.76	1695	—	2.47	—	LC(LS/PDM)	(8,9)
TYC9073-0762-1	281.71897	-62.17684	M1	5.37	-0.73	1999	—	2.57	—	LC(LS/PDM)	(8,9)
V2306Oph	247.57524	-12.66259	M3	119.0	-2.08	1423	—	1.08	—	LC(LS)	(1)

**Table S2** Period measurements for wide binaries including M-type stars.

Name	R.A. (deg)	Decl. (deg)	Type	$P_{\text{rot}}$ (day)	$\log(\frac{1}{P_{\text{rot}}})$ (1/day)	$P_{\text{cyc1}}$ (day)	$P_{\text{cyc2}}$ (day)	$\log(\frac{P_{\text{cyc1}}}{P_{\text{rot}}})$	$\log(\frac{P_{\text{cyc2}}}{P_{\text{rot}}})$	Method	Refs.
BD-022198	114.02947	-3.11076	M1	12.2	-1.09	4197	—	2.54	—	LC(LS)	(1)
GJ1054A	46.9823	-28.21971	M0	7.4	-0.87	1278	—	2.24	—	LC(BTFT)	(5)
GJ1264A	327.27399	-72.10253	M0	6.66	-0.82	1644	—	2.39	—	LC(BTFT)	(5)
GJ15A	4.59535	44.02295	M1	45.0	-1.65	1022	—	1.36	—	CL(GLS)	(3)
GJ182	74.89514	1.78352	M0	4.43	-0.65	1753	—	2.6	—	LC(BTFT)	(5)
GJ2036A	73.38001	-55.86031	M2	2.98	-0.47	1790	—	2.78	—	LC(BTFT)	(5)
GJ234	97.34746	-2.81356	M4	8.1	-0.91	2153	—	2.42	—	LC(GLS)	(4)
GJ3331A	76.70798	-21.58587	M1	13.7	-1.14	1242	—	1.96	—	LC(BTFT)	(5)
GJ494	195.19399	12.37574	M0	2.89	-0.46	1278	—	2.65	—	LC(BTFT)	(5)
GJ521A	204.85043	46.18649	M1	49.5	-1.69	657	—	1.12	—	CL(GLS)	(3)
GJ618A	245.01461	-37.529	M3	57.4	-1.76	1242	—	1.34	—	LC(BTFT)	(5)
GJ676A	262.54668	-51.63698	M0	41.2	-1.61	2737	—	1.82	—	LC(GLS)	(4)
GJ720A	278.82663	45.74404	M0	34.5	-1.54	839	—	1.39	—	CL(GLS)	(3)
GJ752A	289.23024	5.1689	M3	46.0	-1.66	3394	—	1.87	—	LC(GLS)	(4)
GJ84	31.27033	-17.61465	M2	43.9	-1.64	1096	—	1.4	—	LC(BTFT)	(5)
GJ841A	329.42168	-51.00618	M2	1.12	-0.05	1278	—	3.06	—	LC(BTFT)	(5)
GJ867A	339.68989	-20.62114	M1	4.22	-0.63	1461	—	2.54	—	LC(BTFT)	(5)
GJ897A	353.19575	-16.75343	M2	4.83	-0.68	1680	—	2.54	—	LC(BTFT)	(5)
HD42581A	92.64423	-21.86463	M1	27.3	-1.44	3029	—	2.05	—	LC(LS)	(1)
HIP1910	6.03737	-62.18454	M0	1.75	-0.24	1025	—	2.77	—	LC(LS/PDM)	(8,9)
HIP23200	74.89514	1.78352	M0	4.42	-0.65	1597	—	2.56	—	LC(LS/PDM)	(8,9)
HIP36349	112.21398	-30.24703	M1	1.64	-0.21	1904	—	3.06	—	LC(LS/PDM)	(8,9)
TWA13A	170.32175	-34.77931	M1	5.44	-0.74	1250	—	2.36	—	LC(LS/PDM)	(8,9)
V1428Aql	289.23024	5.1689	M3	46.0	-1.66	1204	—	1.42	—	LC(LS)	(1)

**Table S3** Period measurements for close binaries including M-type stars.

Name	R.A. (deg)	Decl. (deg)	Type	$P_{\text{rot}}$ (day)	$\log(\frac{1}{P_{\text{rot}}})$ (1/day)	$P_{\text{cyc1}}^a$ (day)	$P_{\text{cyc2}}$ (day)	$\log(\frac{P_{\text{cyc1}}}{P_{\text{rot}}})$	$\log(\frac{P_{\text{cyc2}}}{P_{\text{rot}}})$	Method	Refs.
ARAnd	26.26363	37.94257	M5	0.11	0.97	3394	—	4.5	—	LC(IO)	(12,13)
CZOri	94.1801	15.40314	M3	0.22	0.66	6241±328	—	4.46±0.02	—	LC(FT)	(14,15)
DQHer	271.87605	45.85905	M3	0.19	0.71	4891	—	4.4	—	LC(O-C)	(16,12,13,15,17)
EXDra	271.05937	67.90341	M2	0.21	0.68	7665	1825	4.56	3.94	LC(O-C)	(18,19)
EXHya	193.10093	-29.24889	M5	0.07	1.17	10475	6935	5.19	5.01	LC(O-C/FT)	(16,12,13,15,17,14)
EXO0748-676	117.14046	-67.75214	M	0.16	0.8	4380	—	4.44	—	LC(O-C)	(13,20)
HTCas	17.55467	60.07652	M5	0.07	1.13	13140	—	5.25	—	LC(O-C)	(15,21)
MVLyr	286.81787	44.01885	M5	0.14	0.86	4197±182	—	4.48±0.02	—	LC(DFT)	(16,12,15,17)
OYCar	151.592	-70.23461	M9	0.06	1.2	12775	2299	5.31	4.56	LC(FT)	(14,15,22)
RRPic	98.90026	-62.64008	M4	0.14	0.84	5110	—	4.55	—	LC(DFT)	(16,12,23,13,15)
RWTri	36.40065	28.09747	M0	0.23	0.63	4015±1095	—	4.24±0.12	—	LC(O-C)	(16,12,15)
SSAur	93.34347	47.74037	M1	0.18	0.74	3869±219	—	4.33±0.02	—	LC(IO)	(16,12,14,15,17)
SUUMa	123.11779	62.60623	M5	0.08	1.12	2190	—	4.46	—	LC(IO)	(12,13)
TIC16320250	231.95199	35.61592	M0	0.26	0.59	3650±365	—	4.15±0.04	—	LC	(24)
TTCrt	173.69657	-11.75844	M0	0.27	0.57	1569±328	—	3.77±0.09	—	LC(FT)	(14,15)
UGem	118.7718	22.0014	M5	0.18	0.75	2043±255	—	4.06±0.05	—	LC(FT)	(14,15)
UXUMa	204.17064	51.91373	M1	0.2	0.71	10950	2591	4.75	4.12	LC(O-C)	(16,12,23,13,15)
V2051Oph	257.07953	-25.80881	M8	0.06	1.2	8030	—	5.11	—	LC(O-C)	(15,25)
V436Cen	168.50024	-37.67993	M9	0.06	1.2	9599±292	—	5.19±0.01	—	LC(FT)	(14,15)
V603Aql	282.22765	0.58413	M4	0.14	0.84	6387±912	—	4.64±0.06	—	LC	(23,13,15)
VWHyi	62.29749	-71.29488	M5	0.07	1.13	3613	—	4.69	—	LC(IO)	(12,13,15,17)
WWCet	2.85322	-11.47867	M5	0.18	0.76	2043±109	—	4.07±0.02	—	LC(FT)	(14,15)
ZCha	121.86563	-76.53352	M5	0.07	1.13	10220	—	5.14	—	LC(FT)	(12,23,15,14,26)

<sup>a</sup> For stars with multiple cycle measurements,  $P_{\text{cyc1}}$  represents the most recent result. For MV Lyr, RW Tri, and V603 Aql, the referenced cycle periods are 11–12 years, 8–14 years, and 15–20 years, respectively; we used the median value of each range as the cycle period and half of the interval as its uncertainty.

**Table S4** Derived parameters for wide binaries including M-type stars.

Name	Type <sub>M</sub>	$M$ ( $M_{\odot}$ )	$R$ ( $R_{\odot}$ )	Type <sub><math>m_s</math></sub>	$m_s$ ( $M_{\odot}$ )	$P_{\text{orb}}$ (day)	$q_{\text{tid}}$	$F_r$	Refs.
GJ1054A	M0	0.61	0.64	M3	0.28	2.11	-1.23e-03	1.29e-03	(5, 27)
GJ234	M4	0.22	0.26	M7	0.11	6058.0	-2.81e-11	2.85e-11	(4, 27)
GJ494	M0	0.56	0.59	M7	0.09	5004.0	-8.17e-11	1.97e-10	(5, 27)
GJ84	M3	0.46	0.5	M7	0.11	6818.0	-4.49e-11	7.81e-11	(5, 27)
GJ841A	M3	0.6	0.63	WD	0.6	1.12	-6.62e-03	4.40e-03	(5, 27)
GJ867A	M0	0.59	0.62	M3	0.32	4.08	-3.47e-04	3.27e-04	(5, 27)

**Table S5** Derived parameters for close binaries including M-type stars.

Name	Type <sub>M</sub>	<i>M</i> (M <sub>⊙</sub> )	<i>R</i> (R <sub>⊙</sub> )	Type <sub>m<sub>s</sub></sub>	<i>m<sub>s</sub></i> (M <sub>⊙</sub> )	<i>P</i> <sub>orb</sub> (day)	<i>q</i> <sub>tid</sub>	<i>F<sub>r</sub></i>	Refs.
DQHer	M3	0.4	0.44	WD	0.6	0.19	-1.35e-01	7.52e-02	(16, 12, 13, 15, 17)
EXDra	M2	0.54	0.57	WD	0.72	0.21	-1.84e-01	1.08e-01	(18, 19)
EXHya	M5	0.11	0.13	WD	0.79	0.07	-1.72e-01	6.53e-02	(16, 12, 13, 15, 17, 14)
EXO0748-676	M	0.44	0.48	NS	2.0	0.16	-3.23e-01	1.31e-01	(13, 20)
HTCas	M5	0.09	0.11	WD	0.61	0.07	-1.07e-01	4.10e-02	(15, 21)
MVLyr	M5	0.3	0.34	WD	0.73	0.14	-1.95e-01	9.15e-02	(16, 12, 15, 17)
OYCar	M9	0.09	0.11	WD	0.64	0.06	-1.37e-01	5.20e-02	(14, 15, 22)
RRPic	M4	0.4	0.44	WD	0.95	0.14	-2.83e-01	1.34e-01	(16, 12, 23, 13, 15)
RWTri	M0	0.35	0.39	WD	0.55	0.23	-7.66e-02	4.18e-02	(16, 12, 15)
SSAur	M1	0.39	0.43	WD	1.08	0.18	-1.83e-01	8.30e-02	(16, 12, 15, 17)
TIC16320250	M0	0.56	0.59	WD	0.67	0.26	-1.25e-01	7.65e-02	(24)
UGem	M5	0.42	0.46	WD	1.2	0.18	-2.18e-01	9.80e-02	(14, 15)
UXUMa	M1	0.39	0.43	WD	0.9	0.2	-1.46e-01	6.99e-02	(16, 12, 23, 13, 15)
V2051Oph	M8	0.15	0.18	WD	0.78	0.06	-3.44e-01	1.37e-01	(15, 25)
V436Cen	M9	0.17	0.2	WD	0.7	0.06	-4.07e-01	1.69e-01	(14, 15)
V603Aql	M4	0.29	0.33	WD	1.2	0.14	-1.88e-01	7.77e-02	(23, 13, 15)
VWHyi	M5	0.11	0.14	WD	0.67	0.07	-1.47e-01	5.72e-02	(12, 13, 15, 17)
WWCet	M5	0.41	0.45	WD	0.83	0.18	-1.91e-01	9.52e-02	(14, 15)
ZCha	M5	0.12	0.15	WD	0.84	0.07	-1.86e-01	7.13e-02	(12, 23, 15, 14, 26)

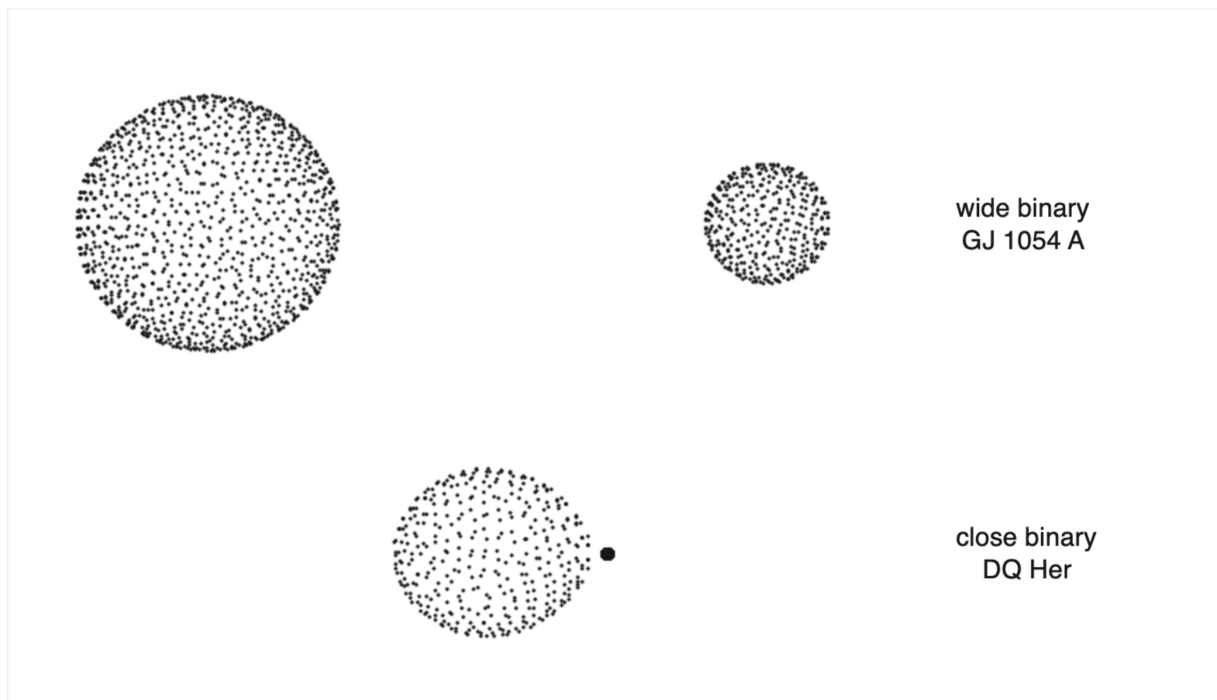


**Figure S1** Examples of mesh plots for two binary systems. The wide binary GJ 1054 A consists of two near-spherical components, while the close binary DQ Her contains a strongly deformed M star. The stellar radii and binary separations are shown to scale.